

## CHAPTER TWO

### 2.1 CYCLIC/FATIGUE LOADING OF STRUCTURAL MEMBERS

Quite a while ago, engineers discovered that if you repeatedly applied and then removed a nominal load to and from a metal part (known as cyclic load), the part would break after a certain number of load-unload cycles; even when the maximum cyclic stress level applied was much lower than the Ultimate Tensile Stress (UTS), and in fact, much lower than the Yield Stress (YS). They discovered as they reduced the magnitude of cyclic stress, the part would survive more before breaking. This behavior became known as “Fatigue” because it was originally thought that the metal got “tired”.

In summary, when a ductile metal is loaded so that the load is gradually increased from zero to a max, final rupture of the material is produced by very large strains. However, if the same material is subjected to repeated loads, failure may occur as a result of stresses much lower than the elastic limit and there will be no plastic deformation in the region of the fractures. Most often, there is usually no prior indication of impending failure. Both tensile and compressive stresses can lead to fatigue damage.

The process of fatigue consists of three (3) stages:

- a) Initial fatigue damage loading to crack nucleation and crack initiation.
- b) Progressive cyclic growth of a crack (crack propagation) until the remaining uncracked cross-section of the part becomes too weak to sustain the loads imposed.
- c) Final, sudden fracture of the remaining cross-section.

#### ***Different types of fatigue/cyclic loading***

There are three (3) different types of fatigue loading:

- 1) zero-to-max-to-zero: Where a part which is carrying no load is then subjected to a load, and later, the load is removed, so the first part goes back to no-load condition. Example: chain used to haul lugs behind a tractor.

- 2) Varying loads superimposed on a constant load: The suspension wires in a railroad bridge are an example of this type. The wires have a constant static tensile load from the weight of the bridge, and an additional tensile load when a train is on the bridge.
- 3) Fully-reversing load: Once cycle of this type of loading occurs when a tensile stress of some value is applied to an unloaded part and then released, then a compressive stress of the same value is applied and released. A rotating shaft with a bending load applied to it is a good example of fully reversing load.

Figure below describes a good example of a member of such loading. The outermost fibres on the shaft surface on the convex side of the deflection (upper surface in the picture) will be in tension, and the fibres on the opposite side will be in compression. The shaft rotated 180 degrees in its bearing, with the load remaining the same. The shaft stress level is the same, but now the fibres which were loaded in compression before rotation are now in tension and vice versa.

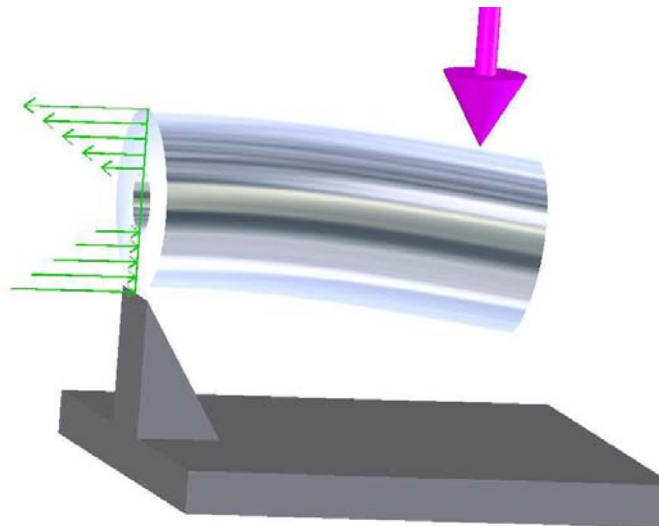


Figure 2.1 – Internal forces of a member under fatigue loading

As a matter, this mechanism of fatigue loading is the type used in laboratory.

### 2.1.1 How cyclic strength of steel is Determined

Figure 2.2 below is a laboratory specimen. These lab samples were optimized for fatigue life. They are machined with the shape characteristics which maximize the fatigue life of steel, and are highly polished to provide the surface characteristics which enable the best fatigue life.



Figure 2.2 – A polished laboratory specimen

A single test consists of applying a known, constant bending stress to a round sample of the material, and rotating the sample around the bending stress axis until it fails. As the sample rotates, the stress applied to any fibre on the outside surface of the sample varies from maximum-tensile to zero to maximum-compression and back. The test mechanism counts the number of rotating (cycles) until the specimen fails. A large number of tests is statistically massaged to determine the expected number of cycles to failure at the stress level.

The cyclic stress level of the first set of tests is some large percentage of the UTS, which produces failure in a relatively small number of cycles. Subsequent tests are run at lower cyclic stress values until a level is found at which the samples will survive 10 million cycles without failure. The cyclic stress level that the material can sustain for 10 million cycles is called the Endurance Limit (EL).

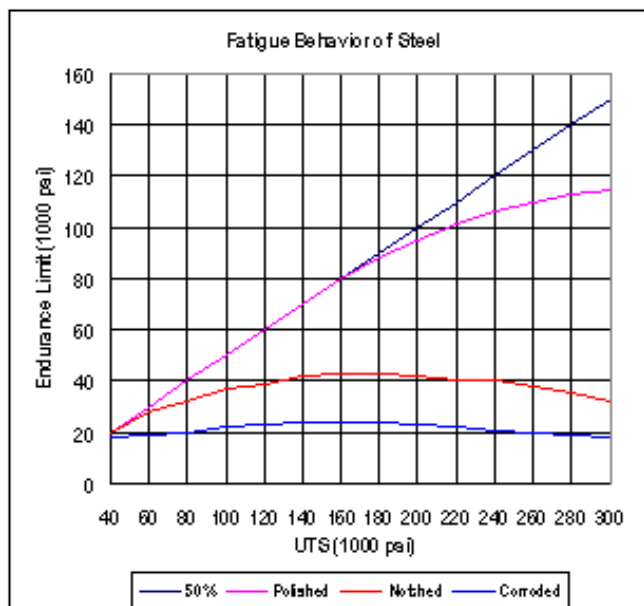
In general stress alloys which are subjected to a cyclic stress level below the EL (properly adjusted for the specifics of the application) will not fail in “fatigue”. That property is commonly known as “infinite life”. Most steel alloys exhibit the infinite life property; but most aluminum alloys as well as steels which have been case-hardened by carburizing, do not exhibit an infinite-life cyclic stress level (EL).

Carburize (case-hardening) – the addition of hardness to the surface of steel by heating the steel in constant with carbon. Heated material is exposed to

carbon then hardened by quenching or cooling slowly, reheating and quenching again. Used on tools which need to retain the resilience of a soft metal to avoid cracking but need a hard surface or when it is simpler or cheaper to shape and carburize a softer material rather than using a harder metal. Cutting tools used for metal latches or milling machines or the centre of a lathe tailstock is usually carburized for wear.

### 2.1.2 Relationship between UTS and Fatigue Strength

Table 2.1 – Endurance limit of polished, notched and corroded steel. The table compares the behaviour of steel surfaces when subjected to fatigue.



It is a rule of thumb that, for steel having a UTS less than 1103 N/mm<sup>2</sup>, the EL for the material will be approximately 45 to 50% of the UTS if the surface of the material is smooth and polished.

A very small number of the special case materials can maintain that approximate 50% relationship above 1103 N/mm<sup>2</sup> level. However, the EL of most steel begins to fall away from the 50% line above UTS of about 1103 N/mm<sup>2</sup> as shown by the line titled “Polished”.

For example, a specimen of SAE-4340 alloy steel, hardened to 32 HRC (Rockwell hardness test) will exhibit a UTS around 1034.1N/mm<sup>2</sup> and an EL

about  $517 \text{ N/mm}^2$ , or 50% of the UTS. If you change the heat treatment process to achieve a hardness of about 50 HRc, the UTS will be about  $1790 \text{ N/mm}^2$ , and the EL will be about  $585.99 \text{ N/mm}^2$  which is only about 32% of the UTS.

Several other alloys known as “ultra-high-strength” steels have seen to have an EL as high as 45% of the UTS at strengths as high as  $2068 \text{ N/mm}^2$ . Also note that these values are EL numbers for fully reversing bending fatigue.

The “notched” line shows the dramatic reduction in fatigue strength as a result of the concentration of stress which occurs at sudden changes in cross-sectional area (sharp corners in grooves, fillets, etc). The EL on that curve is about 25% of the UTS (at around  $1103.04 \text{ N/mm}^2$ ).

The surface finish of the material has a dramatic effect on the fatigue life. That fact is clearly illustrated by the curve “corroded”. It shows that, for a badly corroded surface (fretting, oxidation, galvanic, etc) the EL of the material is, at best, around 15-20% of the material’s UTS.

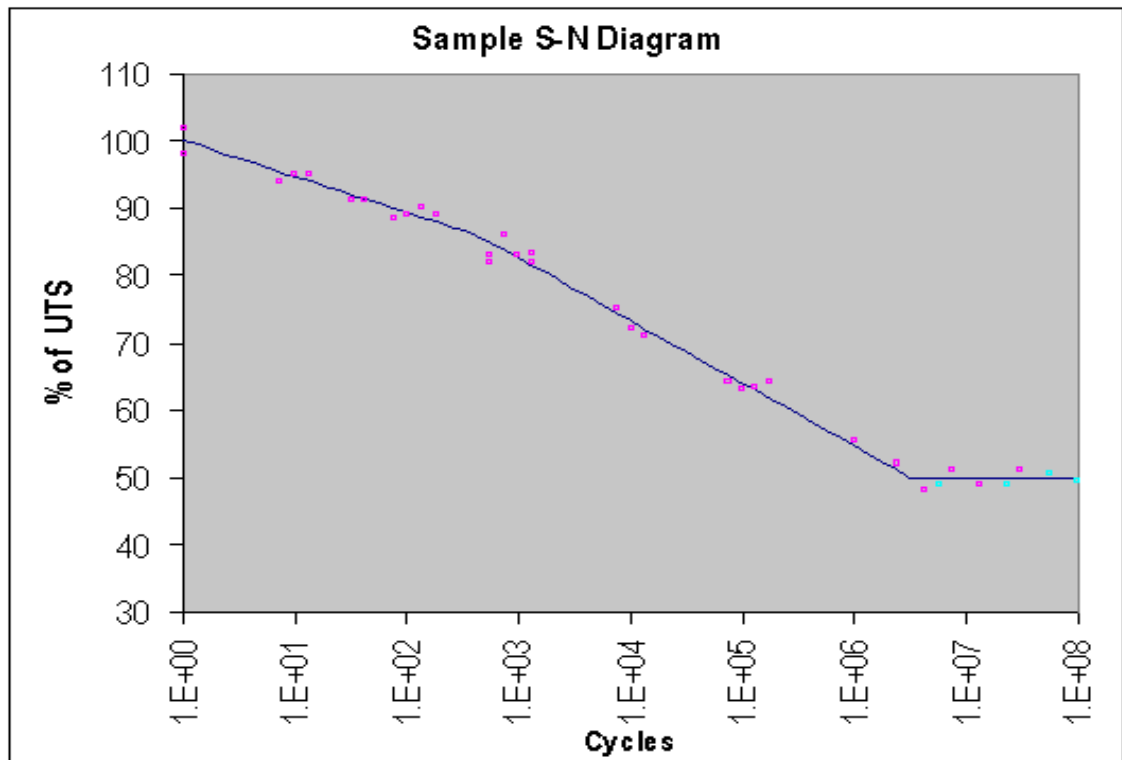
#### 2.1.2.1 Issue of surface on fatigue/cyclic loading

Fatigue failures almost always begin at the surface of the material. The reasons are: The most highly-stressed fibres are located at the surface (bending fatigue) and, the inter-granular flaws which precipitate tension failures are more frequently found at the surface.

The Exactness of the Endurance Line:

It is important to remember that the endurance limit of a material is not an absolute nor fully repeatable number. In fact, every apparently identical sample, cut from adjacent sections in one bar of the steel, will produce different EL values (as well as different UTS and YS) when tested, as illustrated by the stress-number (S-N) diagram in table 2.2

Table 2.2 – Determining the exactness of endurance line



The result shows the result of fatigue tests on a specific material. The tests at each stress level form statistical clusters, as shown a curve is fitted through the clusters of points, as shown.

The curve which is fitted through the clusters, known as an "S-N Diagram", represents the statistical behaviour of the fatigue properties of that specific material at that specific strength level.

The cube-like dots represent the cyclic stress for each test and the number of cycles at which the specimen broke. The circular dots represent the stress levels and the number of cycles applied to specimens which did not fail. The diagram clearly demonstrates the statistical nature of metal fatigue failure.

\*It is recommended to determine what actual EL will be for specific application since experience has it that the values of EL in laboratory tests differ from what they are in actual practice due to the fact that EL values are statistical in nature and determined by optimization.

Real – World allowable cyclic stress =  $K_a \times K_b \times K_c \times K_d \times K_e \times K_f \times EL$

$K_a$  = surface condition; such as polished, ground, machined, as-forged, corroded, etc. Surface is perhaps the most important influence.  $K_a$  could range from 0.80 to 0.90;

$K_b$  = Size; this accounts for changes which occur when the actual size of the part or the cross-section differs from that of the test specimen.  $K_b$  could range from 0.82 to 0.87.;

$K_c$  = Load; Accounts for differences in loading (bending, axial, torsional) between the actual part and the test specimen.  $K_c$  is always at 1.00;

$K_d$  = Temperature; Accounts for reductions in fatigue life which occur when the operating temperature of the part differs from room temperature (the testing temperature). Depending on the temperature  $K_d$  could range from 0.85 to 1.02;

$K_e$  = Reliability; Accounts for the scatter of test data. Example, an 8% standard deviation in the test data requires a  $K_e$  value of 0.868 for 95% reliability and 0.753 for 99.9% reliability. At 99% reliability,  $K_e$  could range from 0.75 to 0.80;

$K_f$  = Miscellaneous; Accounts for reduction from all other effects, including residual stresses, corrosion, plating, metal spraying, fretting and others.

### **2.1.3 Cyclic Material Behaviour**

Stress-Strain response of most materials under cyclic loading is different under single (monotonic) loading. For analysis of notched components it is generally necessary to consider the cyclic material behaviour for strength and life calculations. As mentioned previously, fatigue is a process of crack initiation and growth due to cyclic loading.

- Monotonic Vs True Stress-Strain Curves

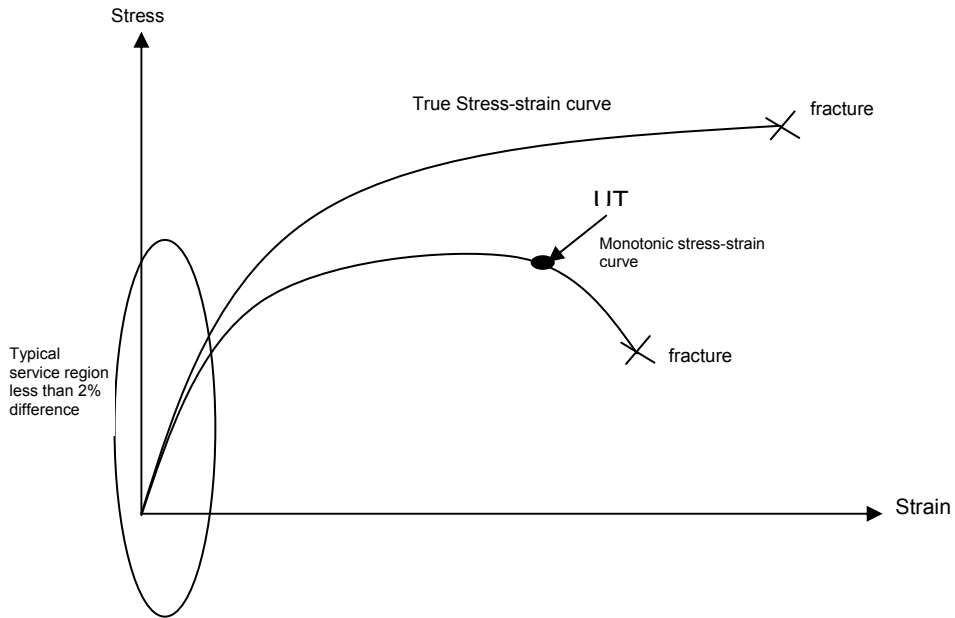


Figure 2.3 – Cyclic material behaviour

### Cyclic Stress-Strain Curve

Considering cyclic loading, only true stress,  $\sigma$  and true strain  $\varepsilon$  are used. However, same engineering values are ignored like (S, e) and true values ( $\sigma, \varepsilon$ )

e = conventional/engineering strain

$$\sigma = S(1 + e)$$

$$\varepsilon = \ln(1 + e)$$

S = Tensile/Compressive Stress

$\sigma$  = stress

$\varepsilon$  = strain

$$\text{For } e = 0.02; \sigma = 1.02S; \varepsilon = 0.0198$$

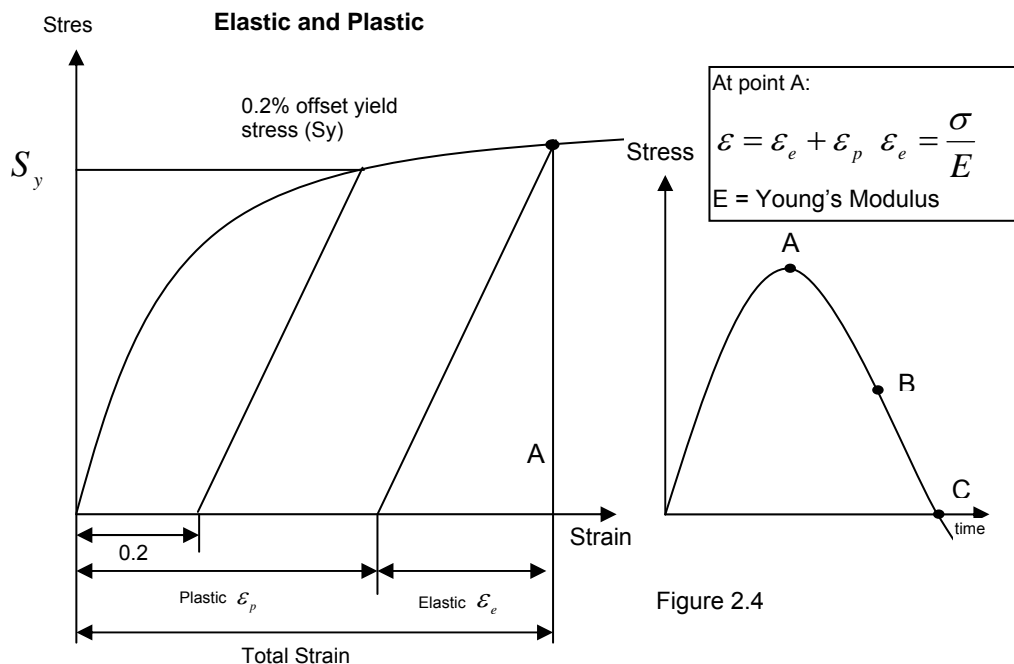


Figure 2.4

## 2.1.4 Cyclic Hysteresis Behaviour

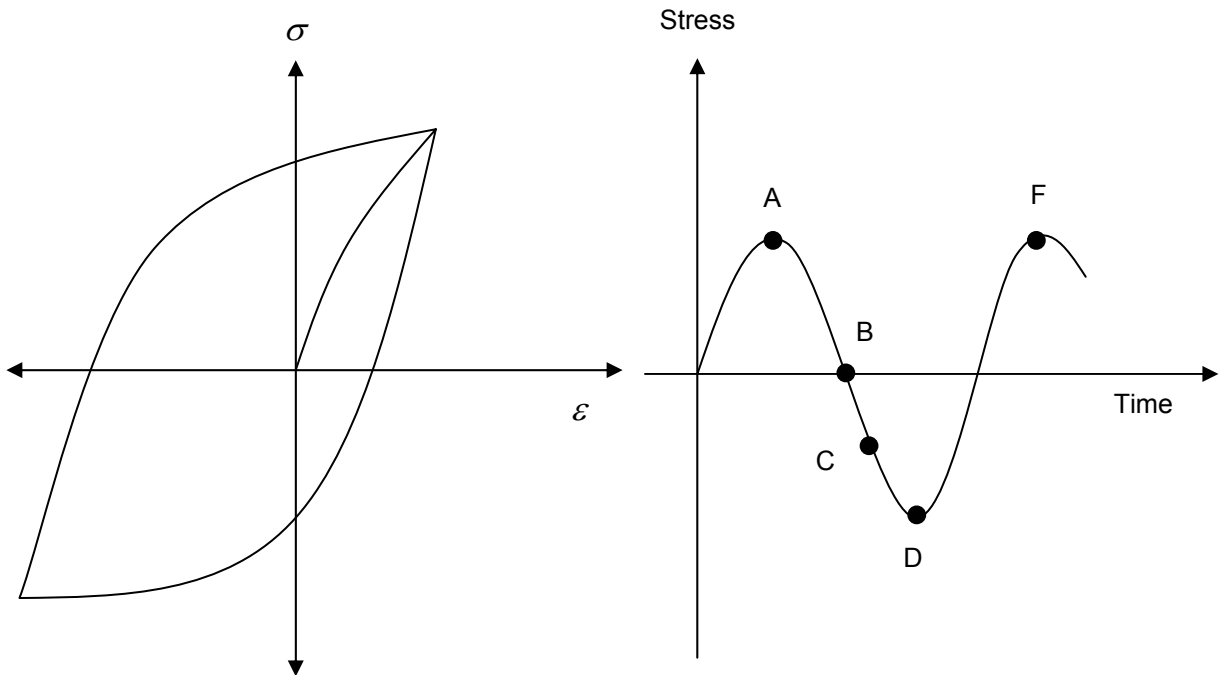


Figure 2.5 – Cyclic hysteresis behaviour

### Cyclic Hysteresis Behaviour

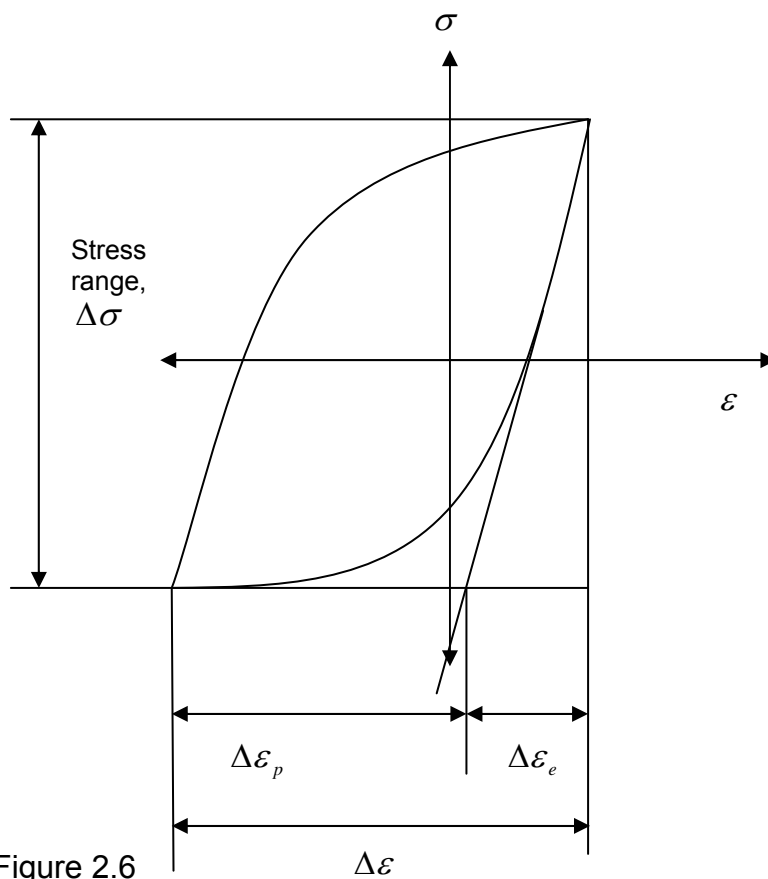


Figure 2.6

Graphically:

*Range*

$$\Delta\epsilon = \Delta\epsilon_e + \Delta\epsilon_p$$

$$\Delta\epsilon_e = \frac{\Delta\sigma}{E}$$

*Amplitude*

$$\frac{\Delta\epsilon}{2} = \frac{\Delta\epsilon_e}{2} + \frac{\Delta\epsilon_p}{2}$$

$$\frac{\Delta\epsilon_e}{2} = \frac{\Delta\sigma}{2E}$$

### Equation for $\sigma$ - $\varepsilon$ Curve:

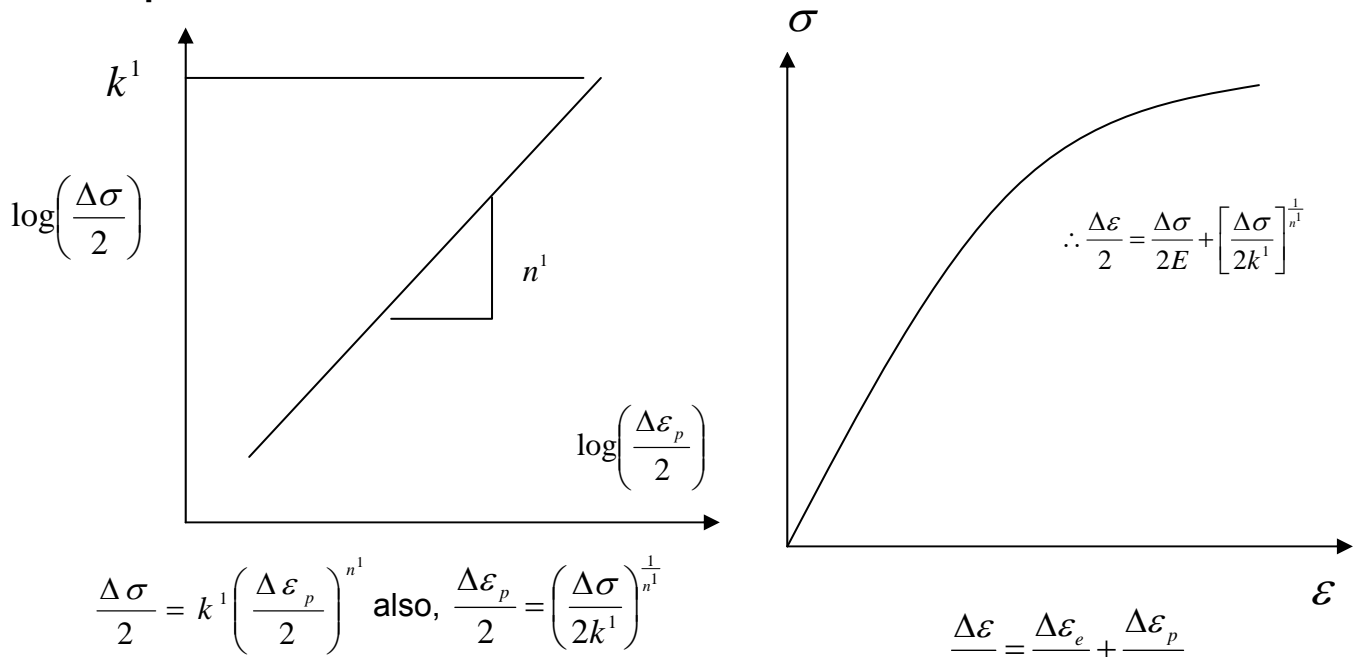


Figure 2.7

$k^1$  = material constant

from eqn:  $\frac{\Delta \varepsilon_e}{2} = \frac{\Delta \sigma}{2E}$

from eqn:  $\frac{\Delta \varepsilon_p}{2} = \left( \frac{\Delta \sigma}{2k^1} \right)^{\frac{1}{n^1}} \quad \therefore \frac{\Delta \varepsilon}{2} = \frac{\Delta \sigma}{2E} + \left[ \frac{\Delta \sigma}{2k^1} \right]^{\frac{1}{n^1}}$

### 2.1.5 Reversed Cyclic Straining

Three hypotheses will be discussed namely:

(I) Bauchinger Effect:

After being plastically strained in one-direction the stress-strain curve of a metal in the opposite sense is lower than the initial stress-strain curve.

Graphically:

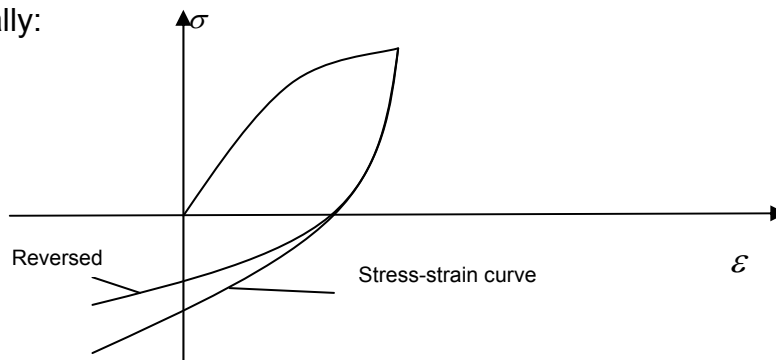


Figure 2.8 – Bauchinger curve

(II) Masings Hypothesis:

Masings suggested (before dislocations were observed) that the stress-strain curve for reversed straining measured from the point of reversal would be the cyclic curve scaled by a factor 2.

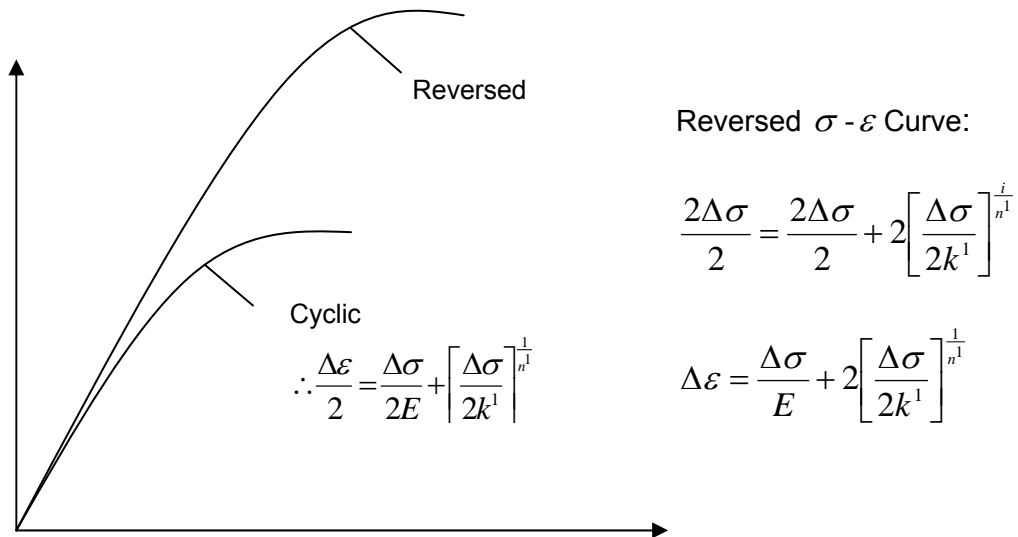


Figure 2.9 – Masings hypothesis

(III) Memory:

The stress for reversed plasticity is generally lowered because of the dislocation pile-ups and their back stresses left by the initial straining. The stress-strain path follows the initial path whenever the prior maximum or minimum strain level is exceeded.

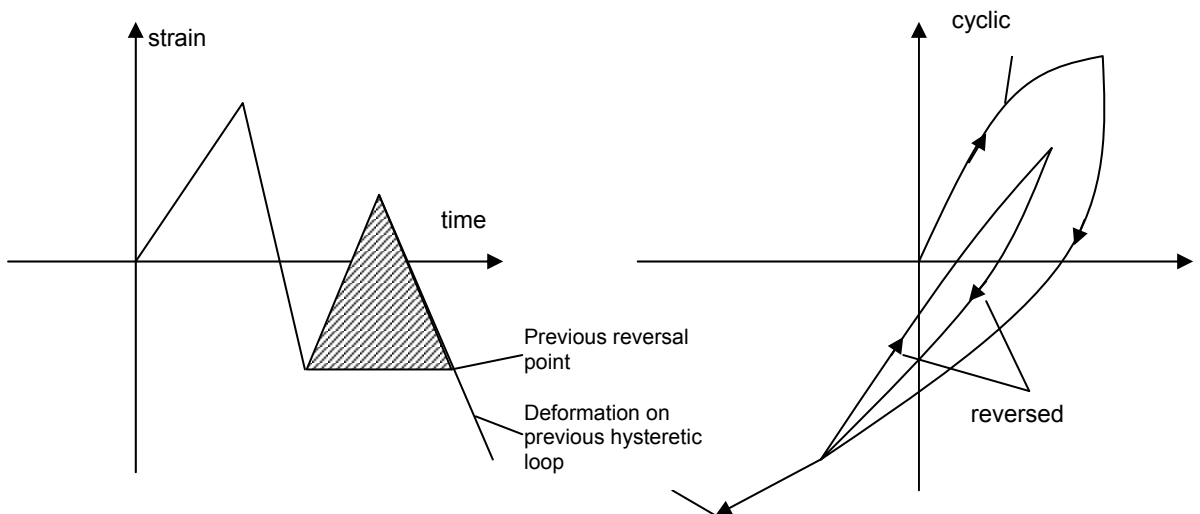


Figure 2.10 – Memory curve

### 2.1.6 Cyclic Crack Growth

Crack growth during uniaxial cyclic deformation occurs by initiation of a micro-crack that propagates on a plane close to that for maximum shear. This is termed a stage 1 fatigue crack. As the crack extends, it rotates from the plane of maximum shear to the plane normal to the principal stress and is then termed a stage 2 fatigue crack.

Fatigue of uncracked metals is traditionally divided into low-cycle and high-cycle fatigue. The transition is usually associated with about 1000 to 2000 cycles to failure. Low-cycle fatigue involves bulk plasticity, whereas deformation in high-cycle fatigue is primarily elastic. The micro-mechanisms of crack of crack growth at stresses in the low-cycle fatigue region are quite similar to monotonic crack growth.

The initial cracks are very small. Their size is not known well because it is difficult to determine when a slip band or other deformation feature becomes a crack. Certainly, however, cracks as small as a fraction of a micron can be observed using modern metallographic tools such as the scanning electron microscope or scanning tunneling microscope. The micro-cracks then grow or link up to form one or more macro-cracks, which in turn grow until the fracture toughness is exceeded. The fatigue failure process can thus be divided into five stages:

- Cyclic plastic deformation prior to fatigue crack initiation.
- Initiation of one or more micro-cracks.
- Propagation or coalescence of micro-cracks to form one or more micro-cracks.
- Propagation of one or more macro-cracks.
- Final failure.

## 2.2 PREVIOUSLY RELATED EXPERIMENTS AND WORKS

The hysteretic behavior of structural members under cyclic loading which is a perfect medium to determine the post-buckling of steel is very important in investigating the dynamic response of members against repeated load, e.g. Earthquake and Wind motion. Generally it is directly related to the collapse of structure under major dynamic motion. Several experiments and numerical analysis have been carried out over the years on steel members under cyclic loading/fatigue to determine several behavioral aspects. Only those works directly related as regards to this review will be mentioned and/or discussed.

**A.H. Salem, M.El Aghoury, F.F. El Dib and M.T. Hanna<sup>7</sup>** determined the ultimate capacity of I-slender columns using a finite element approach. They achieved this by using the state of stress within the section to calculate the effective width and hence the ultimate capacity. A non-linear finite element model was made to investigate the variations of this state of stress along with flange and web width-thickness ratios of slender I-sections for different member slenderness ratios. They tested different groups of slender I-section that varied in their flange and web width-thickness ratios.

### Discussion of results

A non-linear finite element was made using COSMOS/M finite element package. Four node iso-parametric shell element for the model was used. Figure 4 shows an example of the finite element model used:

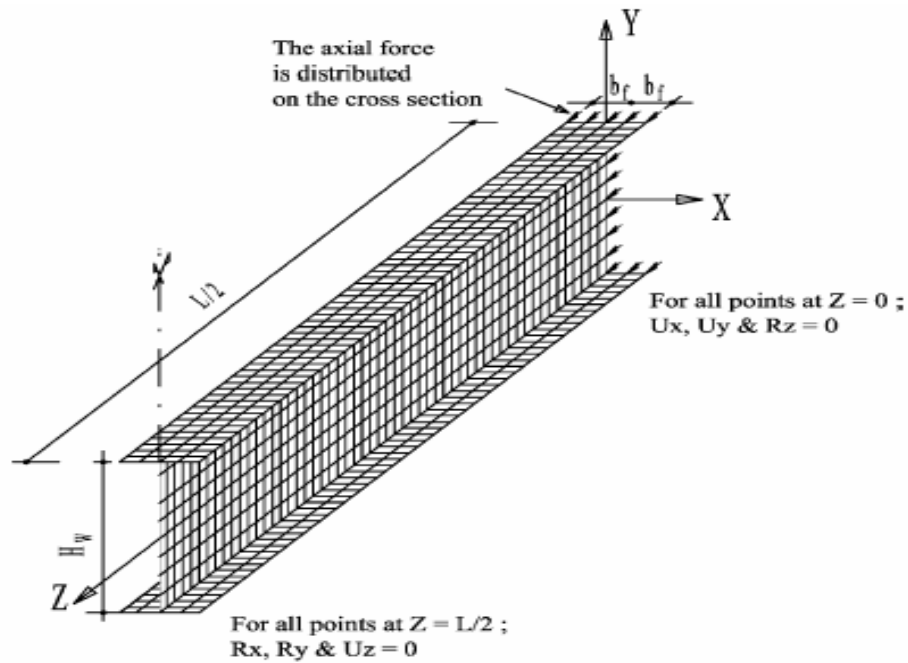
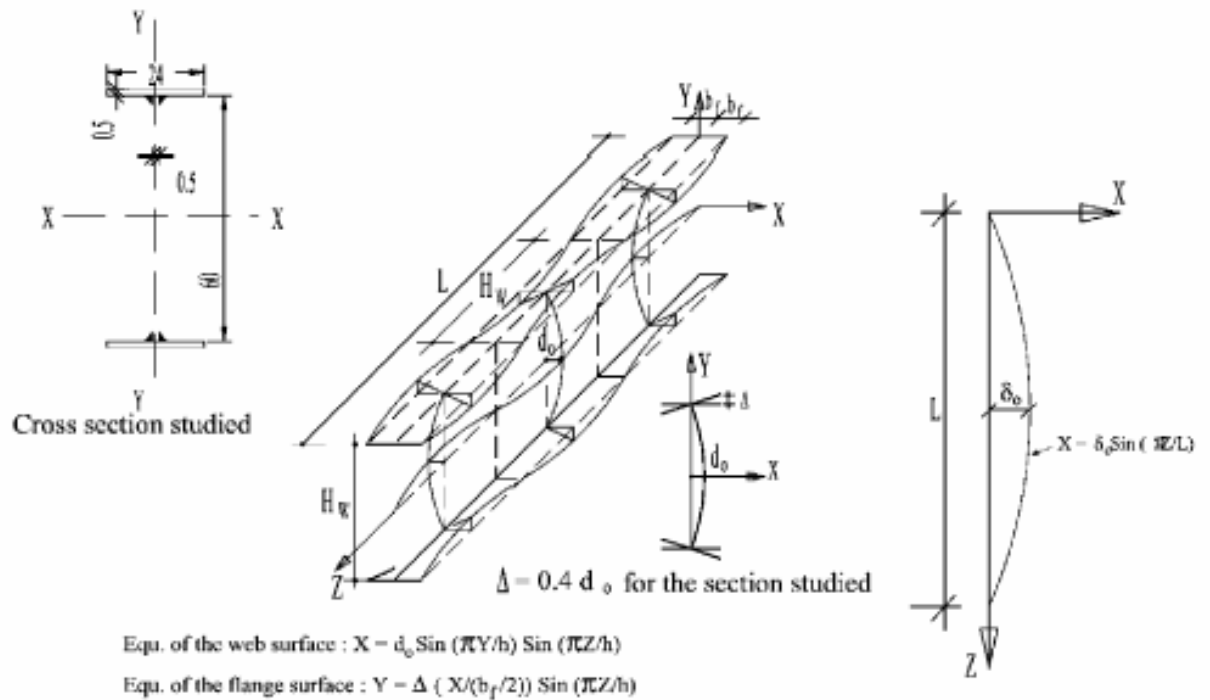


Figure 2.11 – Finite Element Model of Specimen (Courtesy of A.H. Salem et al.)

An I-section column with  $b_f/t_f = 24$ ,  $H_w/t_w = 120$  as shown in Fig. 2.12, and with length equal to 450 cm is selected to study the effect of initial local geometric imperfections. Hancock <sup>(A.H. Salem et al)</sup>, suggested that the distribution of local plate imperfections may be assumed similar to the expected local buckling shape of the plate.

The critical buckling shape consists of a half sine wave in the transverse direction, and series of half sine waves in the longitudinal direction as shown in Fig. 2.12a. Several trials showed that the number of longitudinal half sine waves is approximately equal to the length of the column  $L$  divided by the height of the web  $H^1$  which is similar to the local buckling pattern of a uniaxial loaded plate with length  $L$  and



2.12a – local imperfection mode

2.12b – overall imperfection mode

Figure 2.12 – Initial geometrical imperfections

width  $H$ . This is because the onset of local buckling usually starts from the web since its local buckling stress is smaller than that of the flanges.

The initial local imperfection value,  $d_0$ , ranges from 0.06 cm ( $H/1000$ ) to 1.2 cm ( $H/50$ ). The British steel design code suggested the use of the following formula as an upper limit for the imperfection amplitude,  $d_0$ , of compression steel plates

$$\frac{d_0}{t} = 0.145 \left( \frac{w}{t} \right) \sqrt{\frac{F_y}{E}}$$

Where  $w$  is the width of the plate,  $t$  is the thickness of the plate element,  $w/t$  is the plate width–thickness ratio,  $E$  and  $F_y$  are the material properties of the plate. For the considered section the upper value of  $d_0$  will be 0.3 cm. The maximum initial imperfections value used by Hancock <sup>(A.H. Salem et al)</sup> was  $0.1t$ , which for their section was 0.05 cm. The values of the ultimate axial load  $P$  for different initial local imperfections  $d_0$  was given in Table 2.3.

Table 2.3 - Axial capacity of I-section column with respect to different initial local imperfections ( $b_f=t_f \frac{1}{4} 24$ ,  $H_w=t_w \frac{1}{4} 120$ ,  $L \frac{1}{4} 450$  cm) (Courtesy of A.H. Salem et al.)

Initial imperfection ( $d_0$ )	$H_w/1000$	$H_w/500$	$H_w/250$	$H_w/100$	$H_w/50$
	0.06	0.12 cm	0.24 cm	0.6 cm	1.2 cm
Ultimate axial load (KN)	744.4	738.26	729.27	695.46	645.98

For cases of  $d_0$  ranging from 0.06 to 0.24 cm, the ultimate axial loads were nearly equal (changes from 744.4 to 729.27KN) and a local buckling mode is observed at the ultimate load. This is due to the fact that the ultimate axial load does not depend on the amplitude value of the local buckling wave. For cases of  $d_0$  equal to 0.6 and 1.2 cm the ultimate axial load decreases to be 695.46 and 645.98KN respectively and interactive local–global buckling mode shape was observed at failure load. These values of  $d_0$  (0.6 and 1.2 cm) are high values which cause overall bending about the Y- axis and can not be considered as initial local imperfection values.

Overall imperfections were considered by modeling the member with one half sine wave along its whole length as shown in Fig. 2.12b. The maximum amplitude at the member mid-length was the overall imperfection value. The same section but with different member lengths was selected to study the effect of initial overall imperfections.

The relation between the ultimate axial capacity and the overall imperfection values for different member slenderness ratios were checked and it was clear that the ultimate capacity decreases with increase of the overall imperfection value, and it was more sensitive for members with big slenderness ratios. The ultimate load was not affected by local imperfections whereas it was greatly affected by the overall imperfections. Therefore, in the forthcoming analysis we considered only overall imperfection with a value of  $L/1000$  ( $L = \text{cm}$ ).

#### *Load–displacement relationships*

For each specimen the load–axial shortening and load–lateral displacement of the web mid-point for each stage of loading were reported. Load–axial

shortening represents the axial stiffness of the member studied while the load–lateral displacement of the web mid-point indicates the post local buckling strength gained by the member. Fig. 2.13 represents these relations for an I-section with  $b_f/t_f = 30$  and  $H_w/t_w = 80$ . For members which failed by local buckling mode and those which failed by interactive local–global buckling mode, the load–axial shortening curve was linear with a constant slope up to the local buckling load after which its slope decreases up to the failure load followed by load shedding as shown in Fig. 2.13. The change in the slope of the load–axial shortening curve indicates the reduction in the axial stiffness of the members due to local buckling deformations. The slope of the load–lateral displacement of the web mid-point curve decreases up to local buckling load then increases to failure load showing the post local buckling strength gained by the section. For members that failed by overall buckling the slope of the load–axial shortening curve decreases continuously up to failure load due to the presence of overall deformations. The slope of the load–lateral displacement of the web mid-point curve also decreases continuously up to failure load.

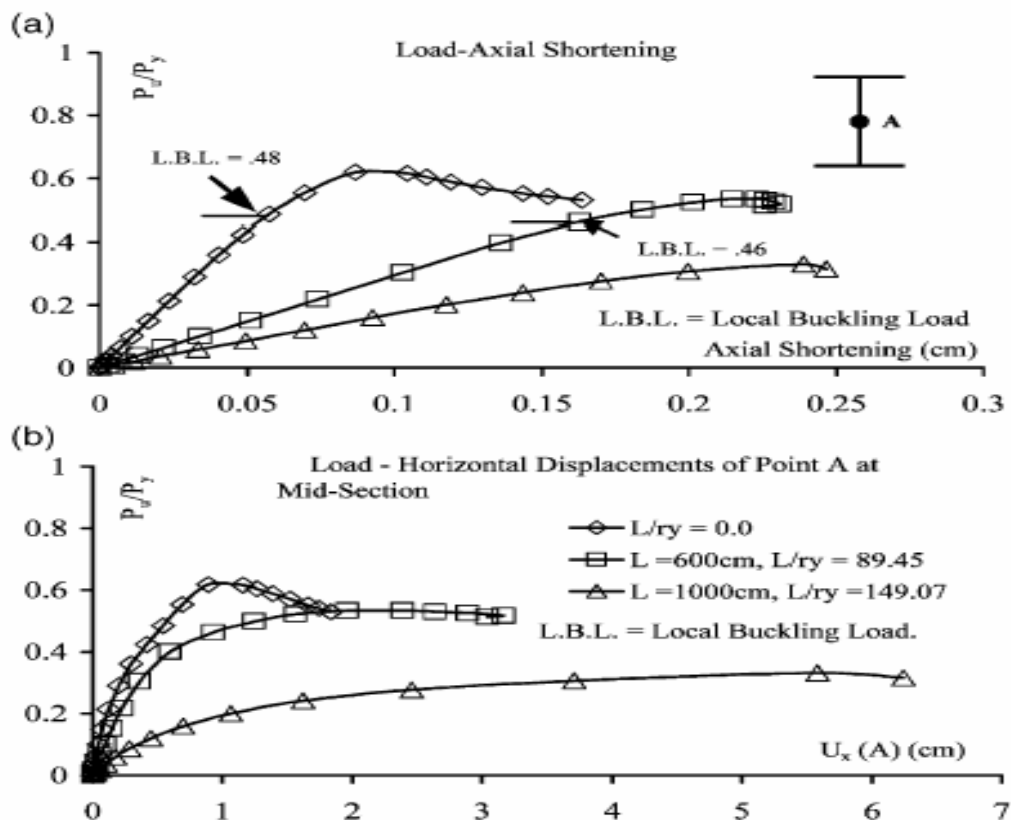


Figure 2.13 – Load-displacement relationships for sections with  $b_f/t_f = 30$ ,  $H_w/t_w = 80$  (Courtesy of Dr. A.H Salem et al.)

Figure 2.14 below shows the deformed shapes for different member slenderness ratios.

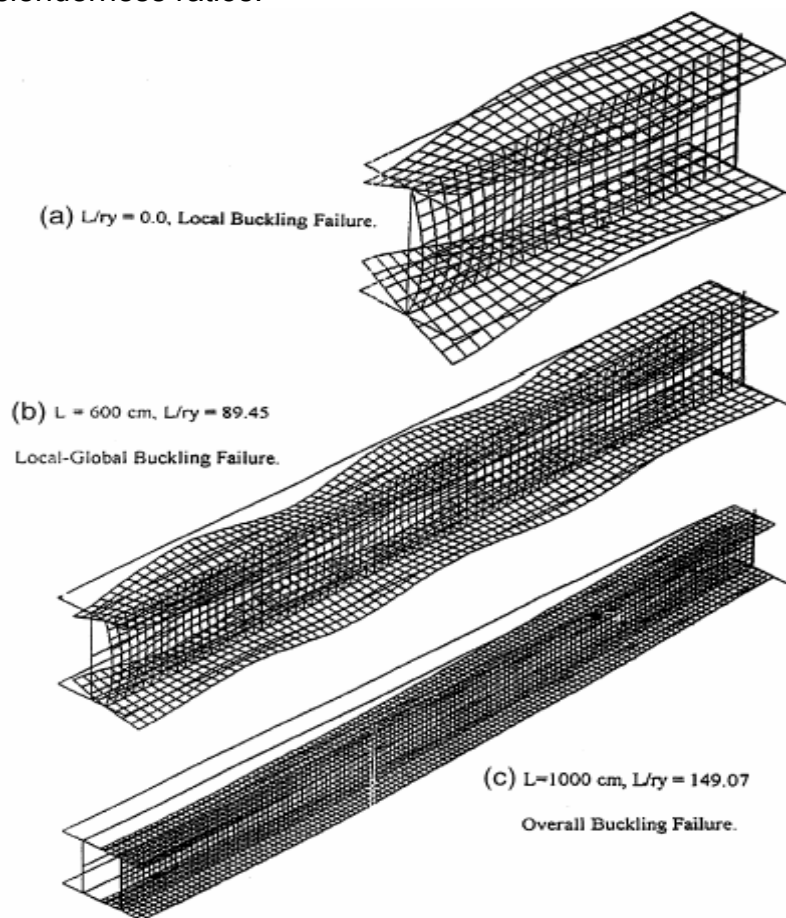


Figure 2.14 – Deformed shapes at failure loads for different member slenderness ratios. (Courtesy of A.H. Salem et al).

### *Stress distribution at failure loads*

Fig. 2.15 shows the stress distribution at failure load of four selected sections for different member slenderness ratios,  $L/r_y$ . These sections have  $b_f/t_f = 15$  and  $30$ , and  $H_w/t_w = 80$  and  $160$ , and were chosen to show the effect of change of the flange, web width–thickness ratio, as well as the member slenderness ratio on the actual stress distribution across the section at failure load.

All members which were prevented from overall out of plane deformations,  $L/r_y = 0$  failed in the local buckling mode. The stress distribution across the sections with  $b_f/t_f = 15$ ,  $H_w/t_w = 80$  and  $160$  was non-uniform across the web and was concentrated near the flange web junction while it was almost uniform

and symmetric on the flanges. This indicates that a local buckling wave occurred in the web only, and due to the compatibility between the flanges and the web, the flanges rotated with the web. However, the stress distribution across the sections with  $b_f/t_f = 30$ ,  $H_w/t_w = 80$  and  $160$ , is non-uniform across the web and is concentrated near the flange web junction. Also, the stresses on the flanges are non-uniform and symmetric about the web. This indicates that the local buckling wave occurred in both the web and the flanges at the same time. Moreover, the stress distribution across the web of section with  $b_f/t_f = 15$ ,  $H_w/t_w = 80$  and  $160$  is different from that of the section with  $b_f/t_f = 30$ ,  $H_w/t_w = 80$  and  $160$  showing the interaction of flange and web width–thickness ratios on the actual stress distribution at failure loads of the slender sections.

When the web width–thickness ratio increases, the stresses at the flange web junction increase while the stresses at the web mid-height decrease. The ratio of the stresses at the flange–web junction to that at the web mid-height reflects the post local buckling strength capacity of the section. From Fig. 2.15 it was clear that the post local buckling strength is more sensitive to web width–thickness ratio than the flange width–thickness ratio. Moreover, as the (slenderness) web width–thickness ratio increases the tendency of the flanges to buckle locally decreases. This appears from the shape of the stresses along the flanges, especially for flange with  $b_f/t_f = 30$ . When  $H_w/t_w = 80$ , the ratio between the maximum stresses at the flange web junction to the minimum stresses at the flange tip is 2.96, while this ratio for the case with  $H_w/t_w = 160$  is 2.16.

Members with intermediate slenderness ratio ( $L/r_y = 88 - 105$ ) failed by interactive local global buckling except those made of sections with  $b_f/t_f = 15$ ,  $H_w/t_w = 80$  which failed by overall buckling. For sections with  $b_f/t_f = 15$ ,  $H_w/t_w = 160$  the local buckling wave occurred in the web only while for sections with  $b_f/t_f = 30$ ,  $H_w/t_w = 80$  and  $160$  the local buckling wave occurred in both web and flanges. The stress distribution across the sections of these members are different from that of members which are prevented from overall out of plane deformations  $L/r_y = 0$  for the same sections due to the presence of overall deformations.

This reveals that the effective width of members that are prevented from overall out of plane deformations may not be suitable for members permitted to overall deformations ( $L/r_y > 0:0$ ).

Members with large slenderness ratio ( $L/r_y = 132 - 158$ ) failed by overall buckling except those made of sections with  $H_w/t_w = 160$  which failed by interactive local–global buckling. The stress distribution shows that buckling waves occurred in the web only for both sections with flange width–thickness ratio,  $b_f/t_f = 15$  and  $30$ .

Below is a table representing the cross-sections that were studied.

Table 2.4 – Cross-sections studied (Courtesy of Dr. A.H Salem et al.)

Cross sections studied						
Sec. no.	$H_w$ (cm)	$t_w$ (cm)	$b_f$ (cm)	$t_f$ (cm)	$H_w/t_w$	$b_f/t_f$
1	30	0.6	9	0.6	50	15
2	30	0.6	12	0.6	50	20
3	30	0.6	14.4	0.6	50	24
4	30	0.6	18	0.6	50	30
5	30	0.5	7.5	0.5	60	15
6	30	0.5	10	0.5	60	20
7	30	0.5	12	0.5	60	24
8	30	0.5	15	0.5	60	30
9	40	0.5	7.5	0.5	80	15
10	40	0.5	10	0.5	80	20
11	40	0.5	12	0.5	80	24
12	40	0.5	15	0.5	80	30
13	60	0.5	7.5	0.5	120	15
14	60	0.5	10	0.5	120	20
15	60	0.5	12	0.5	120	24
16	60	0.5	15	0.5	120	30
17	80	0.5	7.5	0.5	160	15
18	80	0.5	10	0.5	160	20
19	80	0.5	12	0.5	160	24
20	80	0.5	15	0.5	160	30

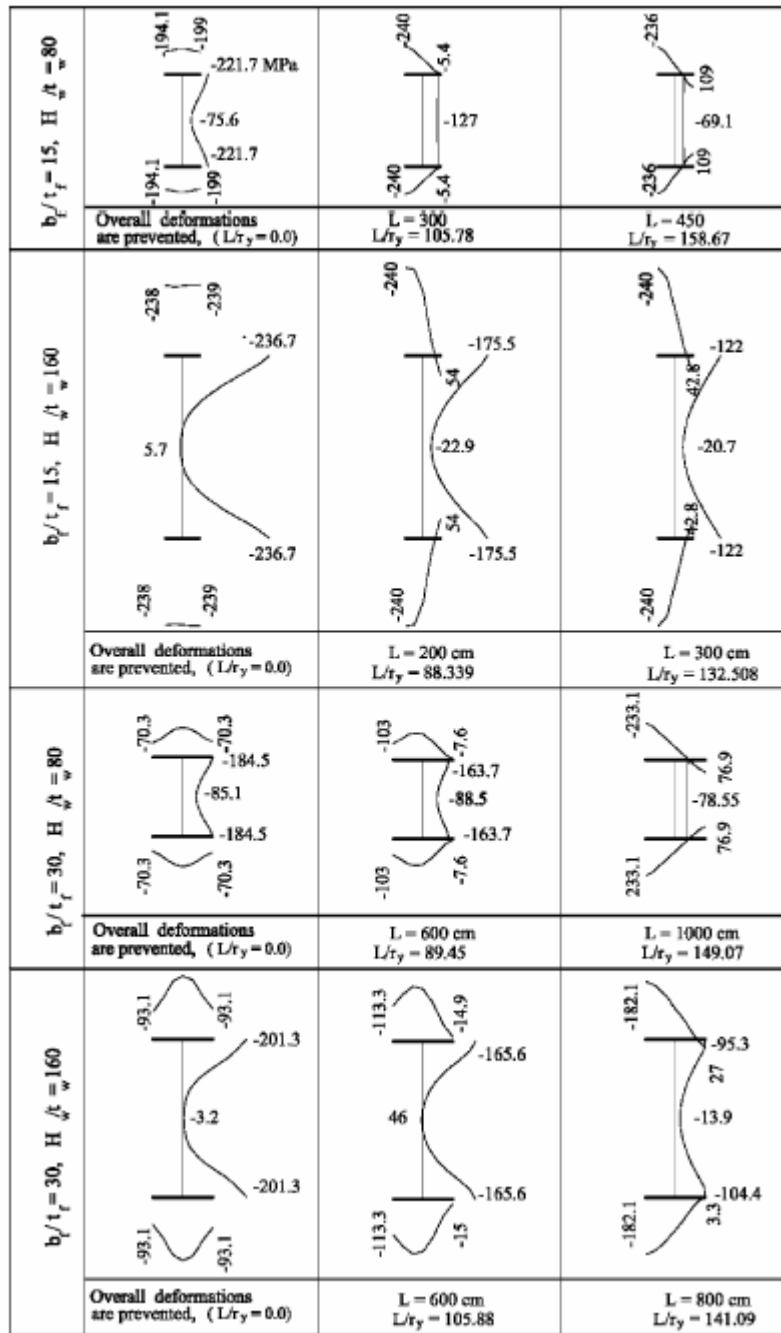


Figure 2.15 – Stress distribution at failure loads across the mid section. (Courtesy of A.H. Salem et al).

#### *Their proposed strength formula*

The finite element results were used to derive an ultimate strength formula by which we can estimate or predict the ultimate axial force of the section. This formula is a function of flange width–thickness ratio,  $b_f/t_f$ , web width–thickness ratio,  $H_w/t_w$ , and member slenderness ratio,  $L/r_y$ .

Sections with flange width–thickness ratio  $b_f/t_f = 15$  and  $20$  and web width–thickness ratio  $H_w/t_w = 50$  and  $60$  did not suffer local buckling deformation before reaching the failure loads and they behaved as compact or non-compact sections. Therefore their results were not considered in deriving the proposed equation.

Firstly, an empirical formula was derived by fitting the normalized ultimate axial loads ( $P_u/P_y$ ) obtained for the case where overall deformations were prevented ( $L=r_y \ 1/4 \ 0:0$ ). The equation that provides a satisfactory fit to the computed maximum strength is as follows:

$$\frac{P_0}{P_y} = \frac{7.5}{\left(\frac{H_w}{t_w}\right)^{0.4} \left(\frac{b_f}{t_f}\right)^{0.2}}$$

Equation A

Where  $P_0 \ 1/4 \ P_u$  for the case  $L/r_y = 0:0$ .

By multiplying Eq. (A) by  $F_y = 240$  MPa, it changed to the following stress equation:

$$\sigma_0(\text{MPa}) = \frac{1800}{\left(\frac{H_w}{t_w}\right)^{0.4} \left(\frac{b_f}{t_f}\right)^{0.2}}$$

Equation B

Then

$$P_0 = \sigma_0 \times A$$

Where  $A$  is the gross area of the section.

The same applies when considering our steel grades, namely 300W, 350W and 460W.

When  $F_y = 300W$ , the stress expression becomes:

$$\sigma_0(\text{MPa}) = \frac{2250}{\left(\frac{H_w}{t_w}\right)^{0.4} \left(\frac{b_f}{t_f}\right)^{0.2}}$$

Equation B1

Also, when  $F_y = 350W$ , stress expression becomes:

$$\sigma_0(MPa) = \frac{2625}{\left(\frac{H_w}{t_w}\right)^{0.4} \left(\frac{b_f}{t_f}\right)^{0.2}} \quad \text{Equation B2}$$

And when  $F_y = 460W$ , stress expression becomes:

$$\sigma_0(MPa) = \frac{3450}{\left(\frac{H_w}{t_w}\right)^{0.4} \left(\frac{b_f}{t_f}\right)^{0.2}} \quad \text{Equation B3}$$

Then the whole ultimate strength curves were fitted with the following interaction formula:

$$\left(\frac{P_u}{P_0}\right)^n + \left(\frac{P_u}{P_E}\right) = 1 \quad \text{Equation C}$$

Where  $P_E$  is the Euler's buckling load equal to  $\pi^2EI_y/L^2$ .

This interaction formula provides that when  $L/r_y = 0:0$ , it gives the results obtained by Eq. (A). Moreover, it is asymptotic to Euler's buckling curve for large values of  $L/r_y$ . The value of the power  $n$  changes the shape of the proposed ultimate strength curve to be fitted with the accurate ultimate strength curves obtained from the numerical results. The value of  $n = 1:5$  gives proper fitting for web width–thickness ratio,  $H_w/t_w$ , between 80 and 160. However, it gives more conservative results for web thickness ratio,  $H_w/t_w$ , below 80.

The advantages of this equation are that the overall section properties are used in determining the ultimate loads of the slender I-sections, and there is no need to calculate the reduced section properties as in the direct strength method. Moreover, it considers the different modes of failure indirectly.

Therefore, the ultimate axial capacity of different columns made of slender I-sections is determined using a non-linear finite element model. Results state that, there is an interaction between flange and web width–thickness ratio along with member slenderness ratio on the actual stress distribution at failure. Moreover, the post local buckling strength of the sections is more sensitive to web width–thickness ratio than flange width–thickness ratio. As the web

width–thickness ratio increases the possibility of flange–web interaction local buckling decreases. Also, flange width–thickness ratio has a remarkable effect on reducing the columns ultimate loads for sections with low web width–thickness ratios. A complete ultimate strength curves were obtained. Comparison with different specifications shows that the concept of effective width gives conservative results due to the conservative prediction of the ultimate stress in the effective width equation. An empirical ultimate strength equation was suggested by fitting the obtained numerical results.

**D. Liu, Nakashima and I. Kanao<sup>6</sup>** did a study on beam hysteretic behavior up to complete failure. Meaning complete fracture (separation) of members at which they cannot provide any resistance whatsoever. This study is needed for the establishment of performance-based design.

The test beams were 1/10-scaled models, and effects of the RBS (reduced beam section) and lateral braces arranged at beam top flanges were examined validating some important similitude and therefore effects of some critical parameters such as local buckling and brittle fracture would not be duplicated. Slenderness ratio of 121 about the weak axis, and its flange and web width-to-thickness ratios were 5.0 and 3.5 respectively. Some of the test specimens were restrained laterally.

Four tests having a combination of standard and RBS beams, with and without lateral braces, were conducted. The lateral braces were adopted to mimic floor slabs and arranged on beam top flanges at discrete locations. The behavior in the large deformation range was commensurate with behavior in many previous study i.e. both standard and RBS beams exhibited both stable and unstable hysteresis, and the lateral braces prevented growth of lateral-torsional buckling using memory method.

They analyzed the beam using the large deformation theory to strengthen the experimental findings. The analysis was able to accurately duplicate the

experimental behavior involving lateral-torsional buckling and succeeding accumulation of out-of-plane deformation.

The RBS failed earlier in the reduced cross-section primarily due to strain concentration at the section. Lateral braces also caused strain concentration leading to earlier failure.

For beams without lateral braces, significant “pinching” and increase in the maximum resistance was observed in the extremely large deformation range. This increase was given as a result of tensile axial forces induced in the beam, which in turn was generated due to its geometry change. The degree of pinching was affected by the length of the beam rigid-zones as well as by the degree of restraint against the beam contraction in its longitudinal direction.

In general, caution will be taken in this experiment and its result because of:

- 1) The reduced scale specimen with a scale-ratio of about 1/10
- 2) The specimen is made of thin plates which are commonly more ductile than thick plates
- 3) Welding which trigger earlier fractures were also avoided in the fabrication of the specimen.

Deformations that correspond to the limit of stable behavior and the instant of complete failure are likely to be smaller in full-scale beams with welded connections than those presented in this study.

\*Pinching – Due to loading and unloading, there might be stiffness and degradation of strength.

Finally, **A. Koursaris and F.O Nghondzweni**<sup>2</sup> conducted simple experiment but detail in nature of analyzing fatigue testing of full-scale Aluminum I-beams.

The aim of the experiment was to establish relationships between the behavior of laboratory samples and that of the actual beam and do micro-analysis of the weld as well as to establish the relationship between micro and macro results under dynamic/cyclic loading.

The test specimen was as follows:

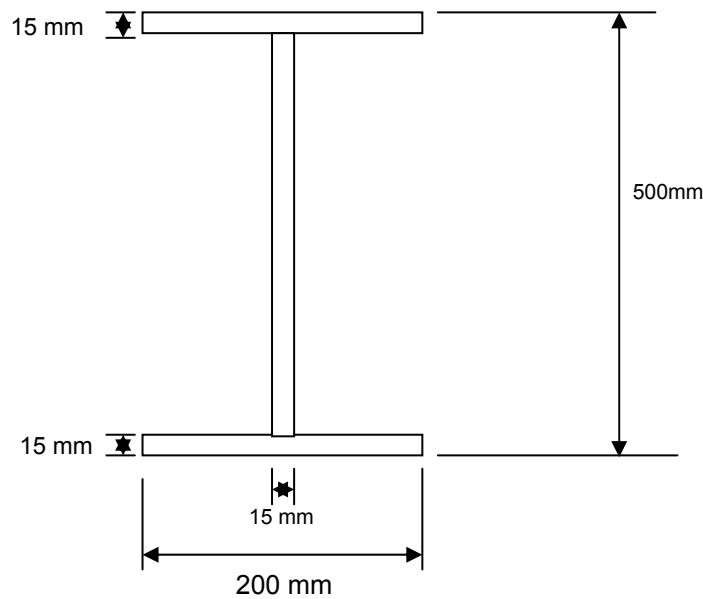


Figure 2.16 – Dimension of I-beam tested

Below is a setup of the experiment which was carried out at the Civil Engineering Laboratory, University of the Witwatersrand, South Africa.

Stresses required for the testing were determined from Section 7, BS 8118: Part 1, 1991.

The table gives the corresponding number of cycles (S-N curves) for different classes of Aluminum.

From the graph, loads were determined using:

$$F = \frac{4z\sigma}{L}$$

where, F = Load in KN

$\sigma$  = Maximum stress in MPa

L = Length of beam in m

$$z = \text{Section Modulus} = \frac{bd^2}{6} - \frac{[(b - t_w)x(d - 2t_f)]^2}{6}$$

After 6 tests, below is a table summarizing the results:

**Table 2.5 – Cumulative Damage Law**

Test	Force, F KN	Max Stress MPa	Predicted Cycles to failure, $N_i$	Cycles applied, $n_i$	$\sum \frac{n_i}{N_i}$
1	140	115	100,000	385,168	3.85
2	160	132	56,000	84,966	1.52
3	180	148	35,000	44,711	1.28
4	200	164	23,000	85,155	3.7
5	220	180	15,000	62,288	4.15
6	230	189	10,000	104,505	10.5

From the experiment, the first crack appeared on one side of the web at 750,000 cycles. The cracks developed at the bottom of the beam and expanded towards loading point.

The set-up is shown diagrammatically below:



Figure 2.17 – Test specimen

It was noted from the experiment that as soon as the crack was visible in the bottom flange, the propagation rate increased dramatically. Failure of the beam occurred 766,793 cycles at the load of 230KN and it occurred at the bottom. From the surface of the fracture, it was deduced that the failure was

due to fatigue which was justified by the smooth fracture surface and the beach marks.

The tensile result showed an average percentage elongation of 12 and 12.5 for the web and flange respectively implying that both web and flange have similar ductility (being of the same material).

However, the UTS of the two parts (flange and web) differed. The UTS of flange was much higher than that of web showing that the flange was stronger. In conclusion of this experiment, the yielding of the specimen far exceeded the predicted/allowable time of fracture primarily due to the large dimensions of the beam. The type of loading (point load system) also contributed to the time and method of failure. The result could have been different if a distributed loading system was used. In other words, any future related experiment should use dimensions much smaller than the one used here (especially if a stronger material is being tested, like steel) and loading system may be altered.

The source of the crack was the stress concentrator caused by the root of the weld due to uneven weld run; so note should be taken during fabrication of specimen for future experiment.